

# JGR Space Physics

## RESEARCH ARTICLE

10.1029/2026JA035129

## Kinetic Structure of an Interplanetary Shock Observed at Two Heliocentric Longitudes



### Key Points:

- We observe a low Alfvén-Mach-number interplanetary shock with a similar shock normal angle at two heliocentric longitudes  $\sim 13^\circ$  apart
- We identify key kinetic features, including downstream magnetic oscillations, ion-acoustic waves, and proton and alpha reflection
- Ion gyro-motion differs significantly between the two downstream regions, producing distinct magnetic profiles and ion-acoustic activity

### Correspondence to:

J. J. Boldú,  
[jordi.boldu@irfu.se](mailto:jordi.boldu@irfu.se)



### Citation:

Boldú, J. J., Graham, D. B., Morooka, M., André, M., Khotyaintsev, Y. V., Dimmock, A., et al. (2026). Kinetic structure of an interplanetary shock observed at two heliocentric longitudes. *Journal of Geophysical Research: Space Physics*, 131, e2026JA035129. <https://doi.org/10.1029/2026JA035129>

Received 22 JAN 2026  
Accepted 5 MAR 2026

### Author Contributions:

**Conceptualization:** J. J. Boldú, D. B. Graham, M. André, Yu. V. Khotyaintsev, A. Dimmock  
**Formal analysis:** J. J. Boldú, D. B. Graham, M. Morooka, M. André, Yu. V. Khotyaintsev, A. Dimmock, A. Lalti, J. Souček, M. Maksimovic  
**Funding acquisition:** D. B. Graham  
**Investigation:** J. J. Boldú, D. B. Graham, M. Morooka, Yu. V. Khotyaintsev, A. Dimmock, A. Lalti  
**Methodology:** J. J. Boldú, D. B. Graham, M. Morooka, M. André, Yu. V. Khotyaintsev, A. Dimmock, A. Lalti, D. Píša, J. Souček, M. Maksimovic, P. Louarn, A. Fedorov, C. J. Owen  
**Project administration:** D. B. Graham, Yu. V. Khotyaintsev

J. J. Boldú<sup>1,2</sup> , D. B. Graham<sup>1</sup> , M. Morooka<sup>1</sup> , M. André<sup>1</sup> , Yu. V. Khotyaintsev<sup>1,2</sup> , A. Dimmock<sup>1</sup> , A. Lalti<sup>3</sup> , D. Píša<sup>4</sup> , J. Souček<sup>4</sup> , M. Maksimovic<sup>5</sup>, P. Louarn<sup>6</sup> , A. Fedorov<sup>6</sup> , and C. J. Owen<sup>7</sup> 

<sup>1</sup>Swedish Institute of Space Physics (IRF), Uppsala, Sweden, <sup>2</sup>Department of Physics and Astronomy, Uppsala University, Uppsala, Sweden, <sup>3</sup>Northumbria University, Newcastle upon Tyne, UK, <sup>4</sup>Institute of Atmospheric Physics of the Czech Academy of Sciences, Prague, Czechia, <sup>5</sup>LESIA, Observatoire de Paris, Université PSL, CNRS, Sorbonne Université, University Paris Diderot, Meudon, France, <sup>6</sup>Institut de Recherche en Astrophysique et Planétologie, CNRS, Université de Toulouse, CNES, Toulouse, France, <sup>7</sup>Mullard Space Science Laboratory, University College London, Surrey, UK

**Abstract** Collisionless shocks convert bulk flow energy into heat, electromagnetic fields, and non-thermal particle populations. Recent studies suggest that downstream magnetic oscillations could play an important role in ion-scale energy dissipation at low-Mach-number shocks; however, the specific shock and plasma parameters involved remain poorly understood. Interplanetary (IP) shocks, often characterized by low Mach numbers, provide an excellent opportunity for investigating these kinetic dissipation mechanisms. We demonstrate, using observations of an IP shock from the Magnetospheric Multiscale (MMS) and Solar Orbiter (SoLO) missions, supported by test-particle simulations, that gyrating protons generate the downstream magnetic oscillations. We found bursts of ion-acoustic waves at the troughs and crests of the magnetic oscillations, suggesting their energy source is related to proton gyration. Comparing MMS and SoLO observations, we conclude that the upstream flow speed to ion thermal speed ratio and magnetic compression ratio are key parameters controlling the ion kinetic behavior that produces downstream magnetic oscillations.

**Plain Language Summary** Collisionless shocks are characterized by abrupt changes in plasma parameters. In the low-collisionality environment of the solar wind, the energy dissipation necessary for the shocks to exist is typically provided by processes involving the electromagnetic fields. Recent research suggests that fluctuations in the magnetic field downstream of the shock transition layer are a key feature of energy dissipation at low-Mach-number shocks. These oscillations have been attributed to gyrating  $\alpha$ -particles at Earth's bow shock. However, observational evidence of these oscillations at interplanetary (IP) shocks has not been conclusively established. We analyze an IP shock using data from the Magnetospheric Multiscale (MMS) and Solar Orbiter (SoLO) missions and combined them with test-particle simulations. We identify key kinetic features associated with the IP shock, including downstream magnetic oscillations, reflection of protons and  $\alpha$ -particles, and periodic bursts of ion-acoustic waves (IAW<sub>S</sub>). Our findings indicate that downstream magnetic oscillations and IAWs are closely linked to the gyration of protons as they transverse the shock, suggesting that ion-scale dissipation is driven by the proton kinetic behavior. Additionally, the differences between the measurements from MMS and SoLO arise from distinct solar wind conditions at both locations, specifically the upstream bulk velocity and the shock's magnetic compression ratio.

## 1. Introduction

Interplanetary (IP) shocks are collisionless shocks that propagate through the heliosphere. They can accelerate particles to MeV energies (Reames, 2001; Trotta et al., 2025; Zank et al., 2007) and trigger extreme space weather events when they interact with planetary magnetospheres (Dmitriev et al., 2005; Gopalswamy et al., 2022). Ion dynamics, particularly at kinetic scales, play an important role in energy dissipation of other types of collisionless shocks, such as planetary bow shocks (Balikhin et al., 2008; Graham et al., 2024; Graham & Khotyaintsev, 2025; Ofman et al., 2009). Similarly, kinetic-scale dynamics are expected to influence the dissipation mechanisms of IP shocks. However, due to their large spatial extent, IP shocks cover a wide range of longitudes, which results in different sections of the shock front interacting with plasma with different properties. These local interactions potentially lead to particles behaving differently along the shock front. Moreover, many processes associated with IP shocks, like particle acceleration (Baring & Summerlin, 2008; Zank et al., 2007) and space weather events

© 2026. The Author(s).

This is an open access article under the terms of the [Creative Commons Attribution License](https://creativecommons.org/licenses/by/4.0/), which permits use, distribution and reproduction in any medium, provided the original work is properly cited.

**Resources:** J. J. Boldú, D. B. Graham, Yu. V. Khotyaintsev, A. Dimmock, D. Piša, J. Souček, M. Maksimovic, P. Louarn, A. Fedorov, C. J. Owen  
**Software:** J. J. Boldú, D. B. Graham, Yu. V. Khotyaintsev, A. Dimmock, A. Lalti, D. Piša, J. Souček  
**Supervision:** D. B. Graham, M. Morooka, M. André, Yu. V. Khotyaintsev  
**Validation:** J. J. Boldú, D. B. Graham, M. Morooka, M. André, Yu. V. Khotyaintsev, A. Dimmock, A. Lalti, D. Piša, J. Souček, M. Maksimovic  
**Visualization:** J. J. Boldú, D. B. Graham, M. Morooka, M. André, Yu. V. Khotyaintsev, A. Dimmock, A. Lalti, D. Piša  
**Writing – original draft:** J. J. Boldú, D. B. Graham, M. Morooka, M. André, Yu. V. Khotyaintsev, A. Dimmock, A. Lalti, D. Piša, J. Souček, M. Maksimovic, P. Louarn, A. Fedorov, C. J. Owen  
**Writing – review & editing:** J. J. Boldú, D. B. Graham, M. Morooka, M. André, Yu. V. Khotyaintsev, A. Dimmock, A. Lalti, D. Piša, J. Souček, M. Maksimovic, P. Louarn, A. Fedorov, C. J. Owen

(Dryer, 1973; Vech et al., 2015), depend on the local shock structure. Therefore, knowing how the local IP shock structure depends on ion kinetics and solar wind conditions is crucial for understanding how they evolve, accelerate particles, and interact with planetary bodies.

Kinetic-scale processes at IP shocks were typically only accessible through high-resolution measurements of the electric and magnetic fields. For instance, the upstream profiles of IP shocks are often characterized by whistler-mode precursors (Tsurutani et al., 1983; Wilson, 2016), IAWs (Boldú et al., 2024), and Langmuir waves (Pulupa et al., 2010). Downstream, magnetic oscillations (Gedalin, 2019; Russell et al., 2009) and IAWs (Wilson et al., 2007) are commonly present. Notably, downstream magnetic compressional oscillations observed at low-Mach-number planetary bow shocks have been attributed to ion kinetic behavior (Balikhin et al., 2008; Gedalin, 2015, 2017; Gedalin et al., 2018; Graham et al., 2024; Ofman et al., 2009). Kinetic-scale measurements at Earth's bow shock confirmed that these oscillations were driven by  $\alpha$ -particles, while protons played a minor role (Graham & Khotyaintsev, 2025).

Given the generally weaker nature of IP shocks (Lalti et al., 2022; Trotta et al., 2025), downstream magnetic oscillations are expected to be generated by ion kinetic processes similar to those observed in low- $M_A$  planetary bow shocks. However, the relation between these oscillations and the kinetic behavior of ions has not yet been conclusively established, owing to a lack of necessary high-resolution ion measurements at IP shocks. Resolving these downstream oscillations is essential for understanding the kinetic structure of IP shocks. Furthermore, as these oscillations are intrinsically linked to the evolution of the ion velocity distribution functions (VDFs), they may be coupled to secondary kinetic phenomena, such as microinstabilities. Finally, it is important to determine whether these ion kinetic processes occur consistently along the shock front or if they are strongly dependent on local solar wind conditions and shock parameters.

To investigate how different sections along the longitudinal extent of an IP shock behave as they encounter solar wind with different properties, we need multiple spacecraft located at similar heliocentric distances, but with enough separation to capture distinct shock segments. Observations of the same IP shock by multiple spacecraft are rare (Burlaga et al., 1981; De Lucas et al., 2011), and those that resolve ion dynamics at kinetic scales are even more uncommon (Cohen et al., 2019). Due to insufficient multi-spacecraft and high-resolution observations, our understanding of the relationship between ion dynamics and the local kinetic structure of IP shocks remains incomplete. To overcome these challenges, we use high-resolution measurements from the Magnetospheric Multiscale (MMS) and Solar Orbiter (SolO) spacecraft, which observed the same IP shock at two different heliocentric longitudes but similar radial distances of 1 au and 0.92 au, respectively. This unique observational configuration enables us to examine how ion kinetic-scale dynamics and local IP shock structure respond to shock parameters and solar wind conditions.

## 2. Observations

On 17 December 2023 at 02:08:52 UTC, SolO (Müller et al., 2020) observed an IP shock at 0.92 au from the Sun. Approximately five hours later, at 07:37:05 UTC and at a heliocentric longitude  $\sim 13^\circ$  from SolO, MMS (Burch et al., 2016) detected the same shock in the solar wind.

Observations from the Solar and Heliospheric Observatory (SOHO) show a coronal mass ejection (CME) directed nearly Earthward approximately 2.5 days before the MMS measurements. This timing suggests that the CME was the source of the IP shock. In Figure 1a, we present a snapshot of the WSA-ENLIL + Cone Model (Odstrcil et al., 2004) to visualize the source and geometry of the IP shock, as well as the locations of SolO and MMS at the time of the observations. Both SOHO and the WSA-ENLIL + Cone Model support the conclusion that SolO and MMS observe the same shock. This conclusion is further supported by the relatively quiet solar wind recorded several hours before the shock encounters, which is also verified by WIND data.

### 2.1. Multi-Spacecraft Data

For SolO magnetic field  $\mathbf{B}$  measurements, we utilize burst-mode data from the Magnetometer (MAG) instrument, which provides 128 samples/second (Horbury et al., 2020). We analyze ion VDFs and moments generated by the Solar Wind Analyzer-Proton Alphas Sensor (SWA-PAS) every 4 s (Owen et al., 2020).

From the Radio and Plasma Wave (RPW) instrument (Maksimovic et al., 2020), we analyze the electric field  $\mathbf{E}$  utilizing the Maximum Amplitude (MAMP) data product provided by the Time Domain Sampler (TDS) (Soucek

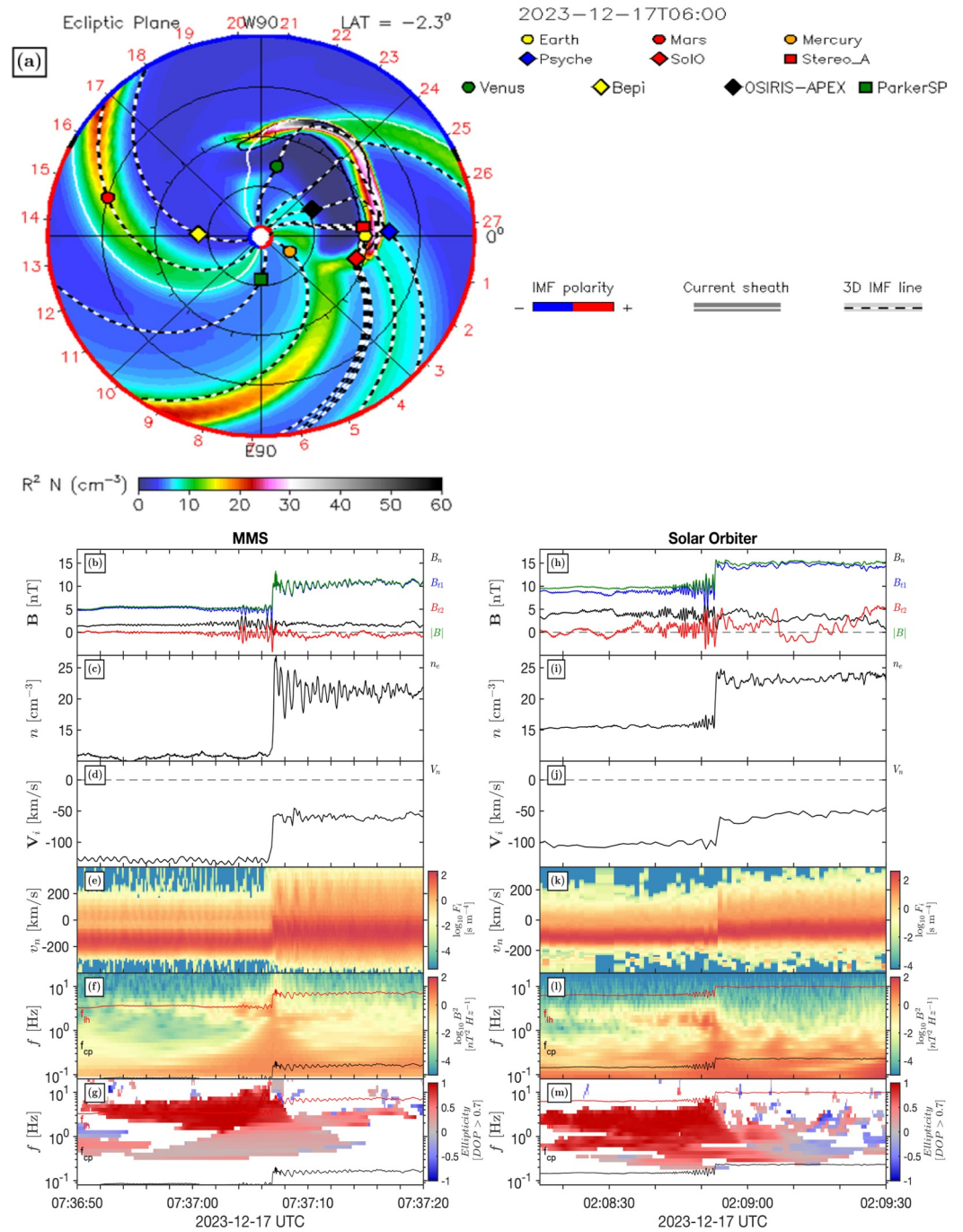


**Figure 1.** (a) Snapshot of the WSA-ENLIL + Cone Model (Odstrcil et al., 2004) simulation output showcasing the configuration of the inner heliosphere on the day of the interplanetary (IP) shock measurements. The color code corresponds to the radially scaled density. Other spacecraft, planets, and interplanetary magnetic field (IMF) lines are displayed for reference. Credit: Community Coordinated Modeling Center (CCMC). (b–m) Overview of the IP shock observations in the normal incidence frame from Magnetospheric Multiscale (b–g) and Solar Orbiter (h–m). (b, h) Magnetic field components ( $\hat{n}$ ,  $\hat{t}_1$ ,  $\hat{t}_2$ ) and magnitude. (c, i) Electron density. (d, j) Ion velocity. (e, k) Reduced ion 1D-VDF along  $\hat{n}$ . (f, l) Magnetic field spectrogram. (g, m) Magnetic field ellipticity. In panels (f, g, l, and m), the proton cyclotron frequency  $f_{cp} = qB/m_p$  (black) and the lower-hybrid frequency  $f_{lh} = \sqrt{f_{cp} f_{ce}}$  (red) are shown for reference.

et al., 2021). These data include the maximum absolute  $\mathbf{E}$  amplitude in the plane of RPW antennas, sampled at 2.0971 MHz and recorded every 7.8 ms, providing 128 samples/second. Additionally, RPW provides electron density ( $n_e$ ) based on the spacecraft potential (Khotyaintsev et al., 2021) at a rate of 256 samples/second.

For the four MMS spacecraft, we employ the Electric field Double Probes (EDP), consisting of data from the Spin-Plane Double Probes (Lindqvist et al., 2016) and the Axial Double Probe (Ergun et al., 2016) instruments, which capture  $\mathbf{E}$  at 8,192 samples/second. We acquire  $\mathbf{B}$  from the Fluxgate Magnetometer (FGM) burst mode, sampled at 128 samples/second (Russell et al., 2016), and ion VDFs from the Fast Plasma Investigation (FPI) sampled every 150 ms (Pollock et al., 2016).

Because FPI does not resolve separate ion species, we compare FPI ion VDFs with data from the Hot Plasma Composition Analyzer (HPCA) instrument (Young et al., 2016) to confirm that the solar wind ion population for this event consists primarily of protons and  $\alpha$ -particles. However, as HPCA is not optimized for the solar wind's cold, collimated beams, its angular and energy resolutions are too coarse to properly characterize the typical solar wind ion VDFs. Therefore, we rely on WIND measurements for proton and  $\alpha$ -particle temperatures ( $T_p, T_\alpha$ ) and alpha-to-proton density ratio ( $n_\alpha/n_p$ ) in our analysis.

We use electron data for the density and estimate bulk velocities of protons and  $\alpha$ -particles from the peaks in the FPI VDFs. Although FPI and HPCA provide comparable angular resolutions, FPI operated in "solar wind" mode during this event. This mode configuration samples a narrowed energy range centered on typical solar wind energies, providing higher energy resolution than the instrument's normal mode and permitting a more detailed analysis of the ion VDFs in the solar wind (Burch et al., 2024; Roberts et al., 2021).

## 2.2. Overview of the Interplanetary Shock

To visualize the shock, we transform the data into the shock-rest normal incidence frame (NIF), using the shock's velocity ( $V_{sh}$ ). In the NIF, the  $\hat{\mathbf{n}}$ -axis aligns with the shock's normal direction. The  $\hat{\mathbf{t}}_2$ -axis is perpendicular to  $\mathbf{B}$  and  $\hat{\mathbf{n}}$ , while  $\hat{\mathbf{t}}_1 = \hat{\mathbf{t}}_2 \times \hat{\mathbf{n}}$ . We estimate the shock-normal direction  $\hat{\mathbf{n}}$  using the mixed-mode methods (Abraham-Shrauner, 1972), which incorporate plasma flow and  $\mathbf{B}$  measurements. We use the jump conditions to calculate  $V_{sh}$  (Smith & Burton, 1988). These methods require selecting appropriate upstream and downstream intervals to compute the desired properties. These intervals and a summary of shock and solar wind parameters for each spacecraft are provided in Table 1.

The shock exhibits a similar shock-normal angle ( $\theta_{Bn}$ ) across the different longitudes. The Alfvén-Mach number ( $M_A$ ) is relatively low at both locations, but larger at MMS. The shock width ( $l_{sh}$ ), defined as the characteristic length of a hyperbolic tangent, is estimated from the  $\mathbf{B}$  time-series, assuming constant  $V_{sh}$ . While  $|\mathbf{B}|$  is greater at SolO, the compression ratio  $B_d/B_u$  is  $\sim 25\%$  larger at MMS. Furthermore, the observations also revealed differences in shock properties and plasma parameters between longitudes, most notably a larger upstream plasma  $\beta_u$  and faster upstream ion velocity at MMS.

The  $\hat{\mathbf{n}}$  in Table 1 is given in Geocentric-Solar-Ecliptic (GSE) coordinates for MMS and equivalently in the Spacecraft Reference Frame (SRF) for SolO. Due to the shock geometry, MMS observes the shock moving radially outward, whereas SolO crosses it from the flank. This results in a significant non-radial  $\hat{\mathbf{n}}$  component at the SolO location, which may partly account for the lower  $M_A$ .

Figures 1b and 1h shows  $\mathbf{B}$  in ( $\hat{\mathbf{n}}, \hat{\mathbf{t}}_1, \hat{\mathbf{t}}_2$ ) coordinates for MMS and SolO, respectively. The shock ramp corresponds to the largest discontinuity in  $|\mathbf{B}|$ . Density and ion velocity moments are shown in Figures 1c, 1d, 1i, and 1j, respectively. Panels (e, k) show reduced 1D-VDFs along  $\hat{\mathbf{n}}$ , which are computed by integrating the VDF over the  $\hat{\mathbf{t}}_1$  and  $\hat{\mathbf{t}}_2$  directions. We note that the instruments sort the particles by energy per charge; however, to convert particle energy to velocity, we use proton mass and charge. Consequently, protons and  $\alpha$ -particles, which in reality have similar upstream velocities, are observed in the 1D reduced VDFs in panels (e, k) at distinct speeds.

## 2.3. Waves Associated With the Interplanetary Shock

Both spacecraft observe electromagnetic waves directly upstream of the shock ramp. The spectrograms in Figures 1f and 1l illustrate the power spectral density of  $\mathbf{B}$  and Figures 1g and 1m the ellipticity, both calculated in the spacecraft frame using the singular value decomposition method (Santolík et al., 2003). Timing the  $\mathbf{B}$  signal

**Table 1**  
*Shock and Plasma Properties*

	MMS	Solo
Shock Parameter		
$M_A$	3.1	2.0
$\theta_{Bn}$ [°]	73	68
$l_{sh}$ [km]	29	35
$l_{sh}/r_{cp,u}$	0.02	0.05
$B_d/B_u$	2.0	1.6
$V_{sh}$ [km/s]	581	371
$\hat{n}$	$[-0.9996, 0.0210, -0.0208]_{GSE}$	$[-0.7382, -0.6480, 0.1875]_{SRF}$
Plasma Parameter		
$n_u$ [cm <sup>-3</sup> ]	11	16
$V_{p,n}$ [km/s]	-130	-113
$V_{\alpha,n}$ [km/s]	-146	-102
$\langle T_{u,i} \rangle$ [eV]	12 <sup>a</sup>	12
$\beta_u$	1.5 <sup>a</sup>	0.7
$\langle V_{n,u}/v_t \rangle$	2.7	2.4
$\Delta B_w$ [nT]	2.4	4.8
$\Delta B_w/ B $	0.45	0.51
Upstream interval	23-12-17T07:36:45/2023-12-17T07:36:50 UTC	2023-12-17T02:08:02/2023-12-17T02:08:12 UTC
Downstream interval	2023-12-17T07:37:12/2023-12-17T07:37:17 UTC	2023-12-17T02:09:00/2023-12-17T02:09:05 UTC

<sup>a</sup>From WIND data.

using the four MMS spacecraft (Vogt et al., 2011), we calculate the phase velocity of the waves in the spacecraft frame and obtain a value of 389[-0.32, -0.16, -0.93] km/s.

In the plasma rest frame, the upstream waves observed by MMS are right-hand polarized with a frequency  $\sim 1.5$  Hz above the lower-hybrid frequency  $f_{lh}$ , consistent with whistler-mode precursors (Wilson, 2016). Minimum variance analysis (Khrabrov & Sonnerup, 1998) yields a propagation direction of the whistler-mode precursors, of [-0.46, -0.34, -0.82], with the sign determined from the timing method. Both the timing and minimum variance analysis methods shows good agreement in the propagation direction. Then, the angle of propagation  $\theta_{kB}$  to the background  $B$  is computed. We estimate  $\theta_{kB}$  to range between 5° near the ramp and 20° further upstream.

Similar waves are observed by Solo, occurring below  $f_{lh}$  in the spacecraft frame. The  $\theta_{kB}$  of these waves ranges from  $\sim 40^\circ$  just in front of the ramp to  $\sim 10^\circ$  further upstream. Although these angles are more oblique, the waves still fall within the typical range for whistler-mode precursors at low- $M_A$  quasi-perpendicular IP shocks, where values are generally  $\lesssim 45^\circ$  (Aguilar-Rodriguez et al., 2011; Blanco-Cano et al., 2016; Kajdič et al., 2012; Wilson, 2016). Moreover, while the absolute amplitude  $\Delta B_w$  of the waves is larger at Solo, the larger  $|B|$  leads to a similar relative amplitude  $\Delta B_w/|B|$  at both locations. These similarities in wave parameters suggest that the waves observed by Solo are also whistler-mode precursors; however, this cannot be confirmed without a proper measurements of low frequency  $E$ , which are not available for Solo at this event.

Next, to visualize the downstream waves, we present, in Figure 2, a zoomed-in view of the downstream regions. In these regions, the shock displays strong high-frequency  $E$  fluctuations, as shown in Figures 2d and 2r, especially at the MMS location. There are no corresponding  $B$  signatures, so we conclude that the waves are electrostatic. For MMS, the plotted  $E$  is bandpass-filtered above 100 Hz. At Solo, we compared the MAMP amplitudes with the triggered snapshot waveforms (SURV-TSWF-E) captured by the RPW/TDS receiver (not shown). The snapshots are consistent with the MAMP amplitudes, confirming that MAMP tracks the envelope of the electrostatic waves.

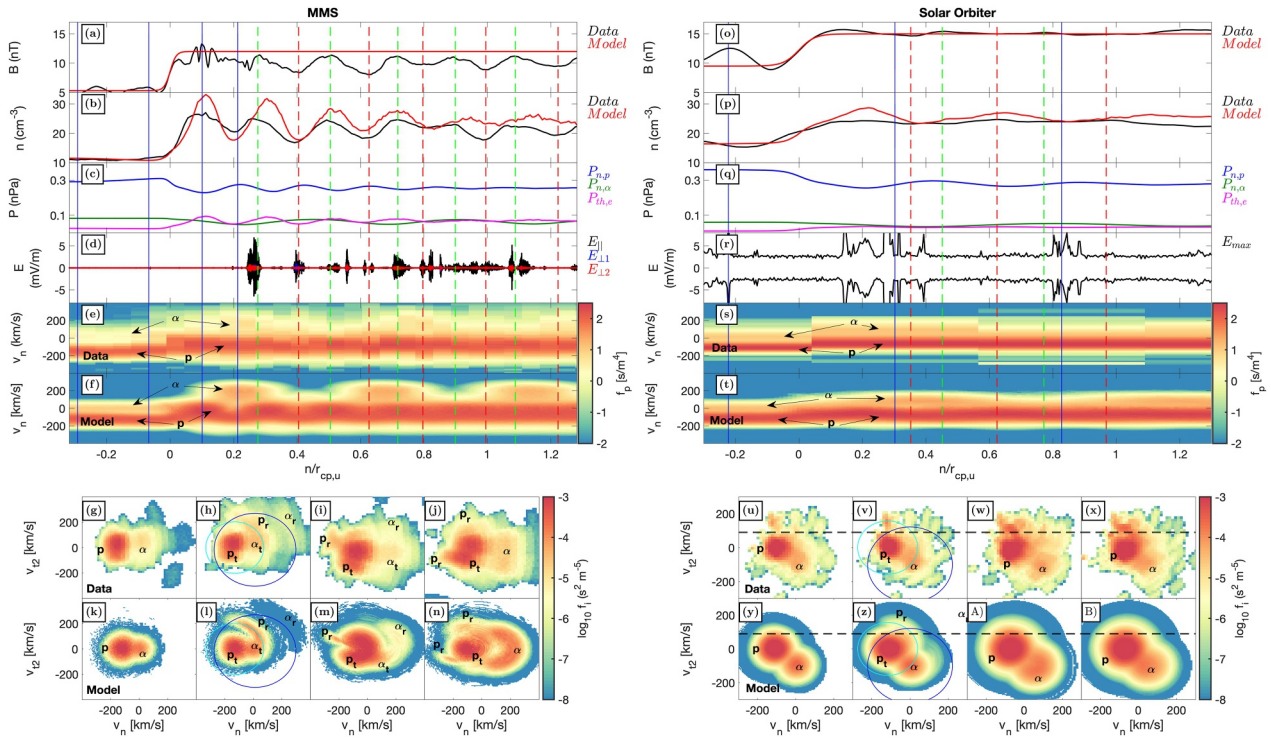


**Figure 2.** Ion motion across the interplanetary shock. The left panels are Magnetospheric Multiscale (MMS), and the right panels are Solar Orbiter (SoLo). (a, o) Measured magnetic field (black) and modeled magnetic profile (red). (b, p) Measured density (black), and density from the test particle simulation (red). Since the model is not self-consistent, the  $\mathbf{B}$  oscillations cannot be obtained, however, density fluctuations are resolved. (c, q) Model results for the plasma pressure. Total pressure for proton (blue) and  $\alpha$  (dark green) are obtained from the model velocity distribution functions (VDFs). Electron thermal pressure (magenta) is obtained from the model  $n_e$  and the prescribed  $P_e$  profile in Equation 6. (d, r) MMS high-pass filtered ( $>100$  Hz) electric field in field-aligned coordinates, and SoLo maximum electric field from the Time Domain Sampler/MAMP data product. (e, s) Measured reduced 1D-VDF along  $\hat{\mathbf{n}}$ . (f, t) Modeled reduced 1D-VDF along  $\hat{\mathbf{n}}$ . (g–j, u–x) Measured reduced 2D-VDF in the  $\hat{\mathbf{n}} - \hat{\mathbf{t}}_2$  plane. (k–n, y–B) Modeled reduced 2D-VDF in the  $\hat{\mathbf{n}} - \hat{\mathbf{t}}_2$  plane. The x-axes represents distance  $n$  taken from a constant  $V_{sh}$  and normalized to the upstream proton convective-gyroradius ( $r_{cp,u} = V_{u,n}/f_{cp}$ ). The labels  $p$  and  $\alpha$  indicate protons and  $\alpha$ -particles, respectively. The indices  $t$  and  $r$  indicate transmitted and reflected populations, respectively. The blue vertical lines in panels (a–f, o–t) indicate the times of the 2D-VDFs. The 2D-VDFs in panels (u, y) are taken at the time of one VDF before the first vertical blue line in panels (o–t). The green (red) dashed vertical lines indicate the crests (troughs) of the downstream  $\mathbf{B}$  oscillations. Above the black-dashed horizontal lines in panels (u–x) Solar Wind Analyzer-Proton Alphas Sensor measurements are unreliable. The time at  $n = 0$  is 2023-12-17T02:08:52.910UTC for SoLo and 2023-12-17T07:37:06.923 for MMS.

We find that these electrostatic waves are characterized by frequencies near the proton plasma frequency in the plasma rest frame. To determine the  $\mathbf{E}$  wave properties at MMS, we use the method developed by Lalti et al. (2023), which relies on spin-plane interferometry. We find that the waves have a phase velocity around the ion-sound speed in the plasma frame. Therefore, we identify these waves as field-aligned IAWs propagating along  $\hat{\mathbf{t}}_1$ .

Ion-acoustic waves are only present downstream from the ramp, with almost no electrostatic activity observed upstream at both shock locations. At MMS, the emissions do not appear as a continuous wave train; instead, they occur in bursts that are spaced periodically. This intermittent pattern of IAW is not evident at SoLo.

Besides whistlers and IAWs, MMS observations display clear downstream  $\mathbf{B}$  fluctuations correlated with  $n_e$  oscillations, as seen in Figure 1b. In the spacecraft frame, these oscillations have a frequency of  $\sim 1.3$  Hz, which lies between the proton-cyclotron frequency and  $f_{lh}$ . Solar Orbiter measurements do not provide clear evidence for these oscillations.

Figure 1g shows that the downstream electromagnetic waves at MMS are linearly polarized, ruling out whistler or ion-cyclotron modes (Gary, 1993; Gurnett & Bhattacharjee, 2017). Using four-spacecraft timing of  $\mathbf{B}$  (Vogt et al., 2011), we estimate the wave's phase velocity  $v_{ph}$  to be  $[-16.1, -39.6, -42.5]$  km/s in the NIF, consistent with a standing wave in the shock rest frame. In contrast, in the plasma frame  $v_{ph}$  is close to  $V_{sh}$  and the fluctuations propagate toward the ramp direction. Additionally, the correlation between  $\mathbf{B}$  and  $n_e$  fluctuations

excludes mirror modes, as these should be anti-correlated (Dimmock et al., 2022; Soucek & Escoubet, 2011). Finally, the presence of these downstream oscillations as a consequence of shock dispersion is not expected for shocks that are not strictly perpendicular (Balikhin et al., 2008; Balogh & Treumann, 2013; Kennel et al., 1985).

We now consider the motion of ions as they cross the shock as the source of the downstream  $\mathbf{B}$  oscillations. In such a case, the wavelength  $\lambda$  of the oscillations is dictated by how long it takes the ions to achieve a gyration, bearing in mind that they are moving along  $\hat{\mathbf{n}}$  at the  $V_n$  speed, so they will not return to the same position in space after one gyration. Thus, for a perpendicular shock,  $\lambda$  is (Balikhin et al., 2008; Graham & Khotyaintsev, 2025; Ofman et al., 2009):

$$\lambda = \frac{|V_{d,n}|}{f_{ci,d}}, \quad (1)$$

where  $f_{ci}$  is the cyclotron frequency of the ion species  $i$ , and  $V_{d,n}$  is the normal component of the downstream ion bulk velocity in the NIF. For oblique shocks,  $\lambda$  depends on the normal component of the magnetic field  $B_n$ . However, for directly transmitted ions, the effect on  $\lambda$  from  $B_n$  is small (Graham & Khotyaintsev, 2025). We calculate for protons,  $\lambda \sim 374$  km, or  $0.23 r_{cp,u}$ , where  $r_{ci,u} = V_{u,n}/f_{ci,u}$  is the upstream ion-convective gyro-radius of the ion species  $i$  (Pope et al., 2019). Using  $f_{c\alpha,d}$ ,  $\lambda \sim 738$  km or  $0.05 r_{c\alpha,u}$ . Now, we estimate the wavelength from the observations  $\lambda_{obs}$  using

$$\lambda_{obs} = \frac{V_{ph,sc}}{f_{wave,sc}}, \quad (2)$$

where the subscript  $sc$  indicates that the quantities are in the spacecraft frame. We find  $\lambda_{obs} = 313$  km or  $0.19 r_{cp,u}$ . This value is close to what is expected from gyrating protons, confirming that the fluctuations at MMS are produced by proton dynamics across the shock. While  $\alpha$ -particles experience a similar motion, as seen in Figures 2f and 2t, their contribution to the oscillations is much less pronounced due to their lower density.

As seen in Figure 1f, the observed frequency of the downstream magnetic oscillations is around an order of magnitude larger than  $f_{cp}$ . The downstream magnetic oscillations are spatial fluctuations that remain stationary (zero-frequency) in the NIF, traveling with the shock at  $V_{sh}$ . Due to the high shock speed relative to the spacecraft compared to  $V_{d,n}$ , the spatial oscillations sustained by the ion gyration are observed at a significantly Doppler-shifted frequency well above the local  $f_{cp}$ . The observed frequency of the downstream magnetic oscillations  $f_{obs}$  in the spacecraft frame is given by:

$$f_{obs} = \frac{V_{sh}}{|V_{d,n}|} f_{ci,d}. \quad (3)$$

Using the measured values, we calculate  $f_{obs} = 1.2$  Hz. This result is in agreement with the  $f_{wave,sc} = 1.3$  Hz spectral peak identified in the  $\mathbf{B}$  observations shown in Figure 1f. We investigate in detail the kinetic origin of these oscillations in the following Section.

### 3. Ion Kinetics Across the Interplanetary Shock

To understand the nature of the downstream  $\mathbf{B}$  oscillations, we analyze the ion kinetics across both shock crossings. To interpret the data and identify processes related to protons and  $\alpha$ -particles, we compare the ion dynamics at MMS and SolO with the test particle model developed in Graham and Khotyaintsev (2025).

We model the shock profile along the distance  $n$  in the  $\hat{\mathbf{n}}$  direction with

$$B_{t1}(n) = -B_0 \tanh\left(\frac{n}{l_{sh}}\right) + B_1, \quad (4)$$

$$n_e(n) = -n_0 \tanh\left(\frac{n}{l_{sh}}\right) + n_1, \quad (5)$$

and

$$P_e(n) = -P_0 \tanh\left(\frac{n}{l_{sh}}\right) + P_1. \quad (6)$$

The jump conditions are taken from observations. The values used for MMS are:  $B_0 = 3.3$  nT,  $B_1 = 8.6$  nT,  $n_0 = 5.1$  cm<sup>-3</sup>,  $n_1 = 16.0$  cm<sup>-3</sup>,  $P_0 = 1.8 \times 10^{-2}$  nPa and  $P_1 = 6 \times 10^{-2}$  nPa. For SolO the values used are:  $B_0 = 2.8$  nT,  $B_1 = 12.2$  nT,  $n_0 = 3.8$  cm<sup>-3</sup>,  $n_1 = 19.8$  cm<sup>-3</sup>,  $P_0 = 1.0 \times 10^{-2}$  nPa and  $P_1 = 2 \times 10^{-2}$  nPa. The magnetic profile of the model is depicted by the red curve in Figures 2a and 2o. The test particle model solves the equations of motion of ions crossing the shock profile in Equations 4–6 and the model  $\mathbf{E}$  is calculated using the generalized Ohm's law (Graham & Khotyaintsev, 2025; Khotyaintsev et al., 2006). In this event, the only ions encountered are  $\alpha$ -particles and protons.

The VDF of each ion species is reconstructed using Liouville's theorem. The individual VDFs are then combined to produce a single VDF series for each spacecraft. Figure 2 shows the model results alongside the observations. The left panels correspond to MMS and the right panels to SolO. The time-series data from the spacecraft are transformed into distance, assuming a constant  $V_{sh}$  and normalized to  $r_{cp,u}$ . Since the instruments cannot differentiate between ion species, we used the proton mass and charge to convert from energy to speed for all ions in Figures 2e and 2s. Then, to compare to instrument measurements, we use Equation 8 in Graham et al. (2024) to transform the modeled VDFs into the spacecraft frame, as shown in Figures 2f and 2t. A detailed explanation of the VDF reconstruction process and the test particle model is given in Appendix A of Graham and Khotyaintsev (2025).

We begin by examining MMS data. Panels (a, b) show  $\mathbf{B}$  and  $n_e$ , respectively. The model (red line) and the measurements (black line) show similar density fluctuations. The model is not self-consistent, so  $\mathbf{B}$  fluctuations are not predicted. However, assuming downstream pressure is constant, the magnitude of  $\mathbf{B}$  can be estimated. Panel (c) shows the total pressure from protons (blue) and  $\alpha$ -particles (dark green). Pressure fluctuations from protons dominate and are anti-correlated with the observed  $\mathbf{B}$  fluctuations, which is consistent with the pressure balance between the plasma and  $\mathbf{B}$ . The total pressure of protons and  $\alpha$ -particles includes the thermal pressure  $P_{th,i}$  and dynamic pressure  $P_{dyn,i} = n_i V_{n,i}^2$ . In both cases,  $P_{dyn,i}$  fluctuations are the dominant component. The electron thermal pressure  $P_{th,e}$  (magenta curve) is derived from the model  $n_e$  and Equation 6.

The model reveals that  $V_n$  and  $n_i$  are in anti-phase, which results in an opposite contribution to  $P_{dyn,i}$ . Furthermore, we note that the model overestimates the  $n_e$  fluctuations, which suggests that the impact of  $P_{dyn,p}$  to the  $\mathbf{B}$  fluctuations is likely more significant than shown.

Panel (e) presents the reduced ion VDFs along  $\hat{\mathbf{n}}$ . Likewise, the resulting 1D-VDF from the model is shown in panel (f). Periodic features are resolved directly downstream of the ramp, consistent with gyrating  $\alpha$ -particles inferred from test-particle results. The model also reveals the gyrating motion of protons, which is not fully resolved by MMS. In Figure 2, we have labeled the different particle populations. The labels p and  $\alpha$  indicate the full proton and  $\alpha$ -particle populations, respectively, while the indices  $t$  and  $r$  denote directly transmitted and reflected populations, respectively.

To gain further insight into the gyrating process, we examine the reduced 2D-VDFs in the  $\hat{\mathbf{n}} - \hat{\mathbf{t}}_2$  plane. Panels (g–j) and (k–n) show the 2D-VDFs from observations and the model, respectively, taken at the times indicated by the blue vertical lines in panels (a–f). We note that compared to the model, the observed VDFs are elongated along  $\hat{\mathbf{t}}_2$ . This is produced by the coarse angular resolution of FPI, which is not designed to measure cold ion beams such as the solar wind.

In panels (g, k), we observe the protons and the  $\alpha$ -particles well separated upstream from the ramp in the spacecraft frame. Closer to the ramp, the model predicts a second proton population around 200 km/s in  $\hat{\mathbf{t}}_2$ . This proton population is identified in Figure 2h, just above the transmitted  $\alpha$ -particles. Similarly, the model reveals the presence of a second population of  $\alpha$ -particles, as seen in Figures 2l and 2m. These are resolved by MMS at the predicted velocities around 300 km/s in  $\hat{\mathbf{n}}$  and 200 km/s in  $\hat{\mathbf{t}}_2$ . Because these populations occupy the velocity space regions associated with specularly reflected ions, we interpret them as reflected protons and  $\alpha$ -particles. The theoretical speed for specular reflection is defined by  $|\mathbf{v} - \mathbf{V}_u| = 2V_{u,n}$  (Burgess & Scholer, 2015; Graham

et al., 2024; Khotyaintsev et al., 2024) and is indicated by dark and light blue circles in panels (h, l) for protons and  $\alpha$ -particles, respectively. Reflected protons from IP shocks have been reported recently (Cohen et al., 2019; Dimmock et al., 2023); however, to our knowledge, this is the first observation of  $\alpha$ -particle reflection from an IP shock.

Next, we analyze the SolO data. Panels (s, t) show the reduced VDFs from observations and the model, respectively. After the transformation to the NIF,  $\alpha$ -particles appear in a different region of velocity space compared to MMS. The test particle results reveal that the shock at SolO still influences the VDF; however, the gyration of ions is not as prominent compared with MMS. The SolO's model results for the different plasma pressure components are shown in panel (q). The total proton pressure is still the dominant component, but its correlation with the magnetic field is not as clear as with MMS.

The 2D-VDFs from SolO observations, taken at the times marked by the blue vertical lines in panels (o–t), are shown in panels (u–x) and from test particle results in panels (y–B). At low solar wind speeds ( $\lesssim 300$  km/s in SRF), SWA-PAS measurements become unreliable (Fedorov, 2020). In the NIF, this corresponds to the velocities above the horizontal black-dashed lines in panels (u–B). The test particle results predict a fraction of reflected protons. Since this population is expected within the SWA-PAS uncertainty level, we cannot confirm its presence.

Now, we address the inconsistencies between our test particle results and the observations. First, the differing amplitude of the density fluctuations and the faster damping in the test particle results likely arise from the lack of self-consistency between the fields and the particles in the code. Furthermore, at MMS the downstream  $\mathbf{B}$  is taken higher than the average observed downstream value to account for the effect of the short-scale  $\mathbf{B}$  enhancement found just behind the ramp. No similar signature is seen with SolO, which is better seen by comparing panels (a, o). The higher normal  $\mathbf{E}$  around the ramp introduced by this signature further decelerates the ions, promoting gyration motion. If that signature was absent, the  $\mathbf{B}$  fluctuation would exhibit a different phase than what was observed. This is confirmed by the test particle results, indicating that short-scale processes close to the ramp are important contributors to the downstream profile.

## 4. Discussion

### 4.1. Whistler-Mode Precursors

Kinetic instabilities driven by specularly reflected protons are known to excite whistler-mode precursors (Wilson et al., 2012); however, these are typically associated with higher  $M_A$  shocks than the studied here. Alternatively, whistler-mode waves can be produced by shock dispersion (Kennel et al., 1985). Assuming that the waves observed by SolO and MMS belong to the same branch, the difference in ion reflected populations do not appear to account for the similar wave properties observed at both locations. This may suggest that ion reflection may not be the primary generation mechanism, pointing instead toward shock dispersion as the main driver of these whistler-mode precursors.

In either case, whistler-mode precursors can influence the upstream ion and electron VDFs. In particular, if these waves contribute to upstream ion heating or solar wind deceleration, they reduce the ratio between the upstream bulk velocity and the thermal speed  $V_n/v_T$ , which leads to damping of the downstream  $\mathbf{B}$  oscillations. The  $V_n/v_T$  ratio is an important parameter for the evolution of the downstream  $\mathbf{B}$  oscillations, as lower values promotes more rapid ion gyro-mixing downstream of the ramp (Balikhin et al., 2008). In this event, we argue that whistler-mode waves do not significantly suppress these oscillations as they remain clearly resolved at MMS and reasonably well reproduced by the model.

### 4.2. Downstream Magnetic Oscillations

The test particle model explains most of the VDFs' features, revealing how the transmitted and reflected proton populations evolve with distance  $n$ . Changes in the VDF, primarily resulting from transmitted protons, produce fluctuations in the dynamic pressure, which in turn lead to  $\mathbf{B}$  oscillations.

In the solar wind, ions move near the  $\mathbf{E} \times \mathbf{B}$ -drift velocity. Upon encountering the shock, their velocity deviates from the  $\mathbf{E} \times \mathbf{B}$ -drift velocity due to deceleration by the normal  $\mathbf{E}$ , and their convective gyroradius decreases because of the higher  $\mathbf{B}$ . These combined effects make the gyrating motion more pronounced downstream, leading to spatial VDF fluctuations that travel with the shock at  $V_{sh}$ . If the shock is approximately stationary, we

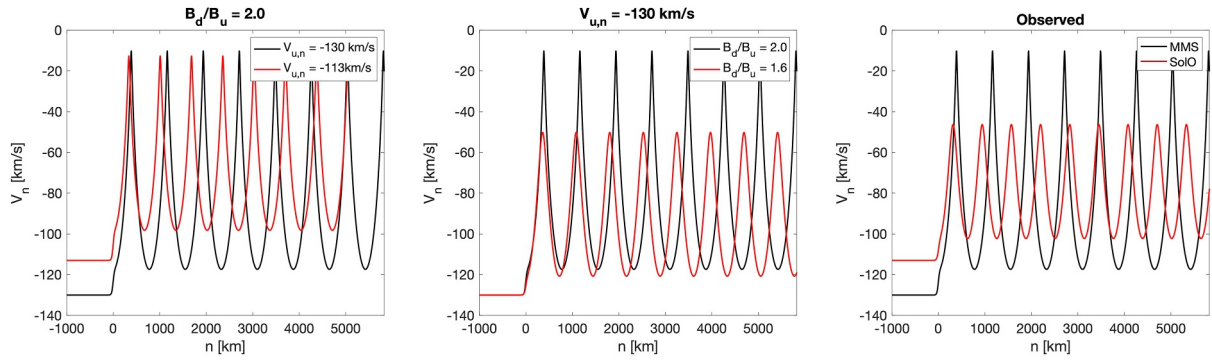


**Figure 3.** Motion of a proton traveling at the bulk speed across the shock based on values from the observation. The values of  $V_{u,n}$  and  $B_d/B_u$  are varied in isolation. (left) Protons with different  $V_{u,n}$  encountering the same shock. (middle) Protons with the same  $V_{u,n}$  encountering a shock with different  $B_d/B_u$ . (right) Motion of protons traveling at the bulk velocity encountering a shock based on parameters observed by Magnetospheric Multiscale (black) and Solar Orbiter (red). Large  $V_{u,n}$  and  $B_d/B_u$  produces more prominent ion cycloid gyration.

can assume pressure balance in the shock rest frame. In this frame, fluctuations in the total plasma pressure  $P_t$  should be anti-correlated with magnetic pressure oscillations (Balikhin et al., 2008; Gedalin, 2016; Gedalin et al., 2015; Graham et al., 2024; Graham & Khotyaintsev, 2025). If electron heating is not significantly greater than ion heating,  $P_t$  fluctuations will be primarily regulated by ion pressure (Gedalin, 2015; Ofman et al., 2009). In the solar wind, the ion pressure is usually dominated by the dynamic pressure  $P_{dyn}$ . The model predicts a  $P_{dyn}$  of protons larger than the other components of  $P_t$  and anti-correlated with  $\mathbf{B}$ . The  $P_{dyn}$  is regulated by the large fluctuations in  $V_{d,n}$  seen in the VDF in Figures 2e and 2f. These results are consistent with protons being responsible of the downstream  $\mathbf{B}$  oscillations through  $P_{dyn}$  fluctuations.

Based on the model results of the peak-to-peak  $P_t$  fluctuations along  $\hat{\mathbf{n}}$  and assuming pressure balance conditions, we estimate downstream magnetic oscillations of  $\sim 3$  nT, which are consistent with MMS observations. Moreover, the amplitude of the  $P_{dyn,\alpha}$  fluctuations corresponds to  $\sim 50\%$  of the proton fluctuations, supporting the conclusion that the main contribution to the fluctuations is from the protons. This contrasts with previous observations of similar downstream oscillations in the Earth's bow shock, where  $\alpha$ -particles dominated the  $\mathbf{B}$  oscillations, possibly due to higher  $n_\alpha$  and proton scattering from  $\mathbf{B}$  turbulence suppressing the proton gyrophase bunching (Graham & Khotyaintsev, 2025).

The density computed from the test particle model using SoLO parameters, plotted in red in Figure 2p, shows short-lived low-amplitude fluctuations due to the same mechanism observed at MMS. Directly downstream, small oscillations are seen in the  $\mathbf{B}$  and  $n_e$  SoLO measurements, depicted by the black lines in 2o, 2p, respectively. These oscillations correspond, following Equation 1 considering protons, to  $\lambda = 279$  km or  $0.35 r_{cp}$ . Timing the peaks of the fluctuations and assuming constant  $V_{sh}$ , we estimate  $\lambda_{obs} = 226$  km or  $0.29 r_{cp}$ . The theoretical value is close to the observed one, suggesting that oscillations occur at SoLO. The main difference is that at SoLO, the fluctuations are damped more quickly or obscured by other processes due to their smaller amplitude.

Downstream  $\mathbf{B}$  oscillations are damped for smaller  $\theta_{Bn}$  (Graham & Khotyaintsev, 2025) and larger thermal speed  $v_t$  relative to  $V_n$  (Balikhin et al., 2008; Gedalin, 2015; Pope et al., 2019). Since the shock at both locations exhibit similar  $\theta_{Bn}$ , the difference in downstream  $\mathbf{B}$  oscillations must arise from another mechanism. Particularly, a small  $V_n/v_T$  ratio causes ions crossing the shock to more rapidly fall out of phase and undergo gyro-mixing due to the broader range of ion velocities. This process smooths the VDF and damps the oscillations. Assuming the downstream  $\mathbf{B}$  oscillations and associated  $n_e$  fluctuations behave like plane waves that decay exponentially with distance, we can analyze the decrease in the relative amplitude of the oscillations ( $\Delta n_e/n_e$ ) as a function of the distance  $n$  to determine the damping rate ( $\gamma$ ). We find that  $\gamma$  at MMS and SoLO is similar, approximately  $-2 \times 10^{-4} \text{ km}^{-1}$ .

Alternatively, the lack of clear downstream  $\mathbf{B}$  oscillations at SoLO may also be attributed to their smaller amplitude. Low  $V_n$  and small  $B_d/B_u$  produce smaller amplitude oscillations. A comparison of these effects is presented in Figure 3. In all panels we show the motion of protons encountering the shock based on values from the observations, and vary  $V_{u,n}$  and  $B_d/B_u$  in isolation. In the left panel, we compare two protons traveling at

**Table 2**  
*Shock Comparison Between MMS and SolO Observations*

Characteristic	MMS	Solo
Whistler-mode precursors	Observed at $f_{sc} \approx f_{lh}$	Observed at $f_{sc} \gtrsim f_{lh}$
Downstream magnetic oscillations	Observed with $\lambda \approx r_{cp,d}$	Not clearly observed
Downstream Ion-acoustic Waves	Intermittent activity matching low-frequency downstream magnetic oscillations	Less activity than MMS; no periodic occurrence
Proton reflection	Predicted in test particle and observed	Predicted in test particle, but not observed due to instrument limitations
$\alpha$ -particle reflection	Predicted in test particle and observed	Not predicted in test particle and not observed

different  $V_{u,n}$  encountering a shock with the same properties. The faster proton exhibits larger oscillations around the guiding center. In the middle panel, we show two protons traveling at the same  $V_{u,n}$ , but crossing a shock with different  $B_d/B_u$ . The proton that crosses the shock with a larger  $B_d/B_u$  has a more pronounced gyromotion. Finally, in the right panel, we show protons traveling at the bulk velocity as seen by MMS and Solo. The combined effects result in a larger cycloid gyration at MMS compared to Solo.

The maximum  $\Delta n_e/n_e$  at MMS is  $\sim 0.3$ , while at Solo  $\Delta n_e/n_e \sim 0.05$ . Likewise, the model also predicts a larger  $\Delta n_e/n_e$  at MMS around 0.4, compared to Solo's of approximately 0.1. Hence, the reason the oscillations are less pronounced at Solo is likely due to their smaller amplitude, which is primarily determined by a  $\sim 15\%$  slower solar wind velocity combined with a  $\sim 20\%$  smaller  $B_d/B_u$  compared to MMS measurements.

### 4.3. Bursts of Ion-Acoustic Waves

The bursts of IAWs observed by MMS occur at the crests and troughs of the downstream  $\mathbf{B}$  oscillations. We have marked the crests and troughs of the  $\mathbf{B}$  and  $n_e$  fluctuations with green and red vertical-dashed lines in Figures 2a–2f and 2o–2t to highlight their corresponding periodicity with the IAW occurrence. In contrast, the IAW signatures at Solo are not as strong as those detected by MMS, and any periodic activity is not evident. This may be related to the downstream  $\mathbf{B}$  oscillations not being as prominent at Solo.

Possible generation mechanisms for IAWs downstream of IP shocks include ion-ion instability between protons and  $\alpha$ -particles (Graham et al., 2025; Liu et al., 2019), beam instability between reflected and directly transmitted protons (Gary, 1978; Wu et al., 1984), and current instability enhanced by fluctuations in the VDFs of ions and electrons (Boldú et al., 2024). Notably, the current-driven instability may be influenced by the same ion kinetics responsible for the  $\mathbf{B}$  fluctuations. The current-driven instability depends on the drift velocity between protons and electrons, and the electron-to-proton temperature ratio. Measurements from MMS reveal fluctuations in the electron VDFs, which potentially alter the instability thresholds. Since the changes in electron and ion VDFs are periodic, they lead to periodic bursts of IAWs, creating a direct link between the downstream  $\mathbf{B}$  oscillations and the electrostatic waves.

## 5. Summary and Conclusion

We use multi-spacecraft measurements to investigate an IP shock observed at two heliocentric longitudes by Solo at 0.92 au and MMS at 1 au. The main characteristics of the IP shock observed at both spacecraft locations are summarized in Table 2. The shock has a similar  $\theta_{Bn} \approx 68^\circ\text{--}73^\circ$  and relatively low  $M_A \approx 2\text{--}3$  in both locations. The upstream profiles are also comparable, including whistler-mode precursors at MMS and similar electromagnetic wave activity at Solo.

However, despite these similarities, we observe significant differences in the downstream profile. At the location of MMS, we observe the reflection of both protons and  $\alpha$ -particles, marking the first detection of  $\alpha$ -particles reflected from an IP shock. Here, the shock is also characterized by compressional downstream  $\mathbf{B}$  oscillations and IAWs bursts that occur at intervals matching the period of the  $\mathbf{B}$  oscillations. Conversely, at Solo's location, no ion reflection is observed, and the downstream  $\mathbf{B}$  oscillations are not evident. Moreover, the IAWs activity is significantly reduced at the shock crossing observed by Solo, lacking any clear periodic pattern.

We find that the downstream **B** oscillations observed by MMS are caused by the gyro-bunching of protons directly transmitted through the shock. In contrast, the downstream **B** oscillations are generated at a smaller amplitude at SolO's location, likely due to a  $\sim 15\%$  lower  $V_n$  and  $\sim 20\%$  smaller  $B_d/B_u$ , which explains why these oscillations are not evident in the SolO observations.

Our observations also suggest a potential connection between the downstream **B** oscillations and the IAWs. This connection is related to the **B** oscillations corresponding to fluctuations in the downstream VDFs, which in turn alter the thresholds of the instabilities driving the IAWs. Overall, we conclude that the observed differences between the spacecraft are due to the local IP shock structure being significantly influenced by the ion kinetic behavior. Likewise, the ion kinetic behavior is highly sensitive to local solar wind parameters and  $\hat{n}$  relative to the upstream ion velocity.

We demonstrate that different sections of the same IP shock exhibit distinct microphysical processes. Our results directly link upstream solar wind conditions to local shock structure through the kinetic behavior of ions, which also manifests as high-frequency IAWs and reflected protons and  $\alpha$ -particles. These findings advance our understanding of the complex, spatially dependent nature of IP shocks and their impact on the heliosphere.

### Conflict of Interest

The authors declare no conflicts of interest relevant to this study.

### Availability Statement

Solar Orbiter is a space mission of international collaboration between ESA and NASA. Solar Orbiter data are available at <http://soar.esac.esa.int/soar/>. For electric field measurements, we used RPW snapshot data sets (Maksimovic, 2020). For ion and electron data, we use SWA data sets (Owen, 2020). For magnetic field measurements, we used burst mode MAG data sets (Horbury, 2020). Data from MMS are available at <https://lasp.colorado.edu/mms/sdc/public/> and <https://spdf.gsfc.nasa.gov/pub/data/mms/>. We use burst mode magnetic field data from FGM (Russell, 2022), and electric field data from EDP (Ergun, 2022). For ion data, we use burst mode distributions from FPI (Gershman et al., 2022b), and burst mode moments from FPI (Gershman et al., 2022a). The data analysis was performed using the irfu-matlab software package. The scripts required to generate the test particle model are available at Graham (2024) and described in Graham and Khotyaintsev (2025). The WSA-ENLIL + Cone Model (Odstrcil et al., 2004) simulation output was retrieved from <https://kauai.ccmc.gsfc.nasa.gov/DONKI/view/WSA-ENLIL/28169/1> using the Space Weather Database Of Notifications, Knowledge, Information (DONKI) catalog, which has been made available by the Community Coordinate Model Center (CCMC).

### Acknowledgments

This work was supported by the Swedish National Space Agency (SNSA). DP and JS were supported by the Czech Science Foundation under the Grant 22-10775S. Solar Orbiter Solar Wind Analyser (SWA) data are derived from scientific sensors which have been designed and created and are operated under funding provided in numerous contracts from the UK Space Agency (UKSA), the UK Science and Technology Facilities Council (STFC), the Agenzia Spaziale Italiana (ASI), the Centre National d'Etudes Spatiales (CNES, France), the Centre National de la Recherche Scientifique (CNRS, France), the Czech contribution to the ESA PRODEX programme, and NASA. Solar Orbiter SWA work at UCL/MSSL is currently funded under UKRI and UKSA Grants UKRI1204, ST/W001004/1 and UKRI1919.

### References

- Abraham-Shrauner, B. (1972). Determination of magnetohydrodynamic shock normals. *Journal of Geophysical Research*, 77(4), 736–739. <https://doi.org/10.1029/JA077i004p00736>
- Aguilar-Rodríguez, E., Blanco-Cano, X., Russell, C. T., Luhmann, J. G., Jian, L. K., & Ramírez Vélez, J. C. (2011). Dual observations of interplanetary shocks associated with stream interaction regions. *Journal of Geophysical Research (Space Physics)*, 116(A12), A12109. <https://doi.org/10.1029/2011JA016559>
- Balikhin, M. A., Zhang, T. L., Gedalin, M., Ganushkina, N. Y., & Pope, S. A. (2008). Venus express observes a new type of shock with pure kinematic relaxation. *Geophysical Research Letters*, 35(1). <https://doi.org/10.1029/2007GL032495>
- Balogh, A., & Treumann, R. A. (2013). *Physics of collisionless shocks: Space plasma shock waves*. Springer Science and Business Media.
- Baring, M. G., & Summerlin, E. J. (2008). Particle acceleration at interplanetary shocks. In *Aip conference proceedings* (Vol. 1039, pp. 240–245).
- Blanco-Cano, X., Kajdič, P., Aguilar-Rodríguez, E., Russell, C., Jian, L., & Luhmann, J. (2016). Interplanetary shocks and foreshocks observed by stereo during 2007–2010. *Journal of Geophysical Research: Space Physics*, 121(2), 992–1008. <https://doi.org/10.1002/2015ja021645>
- Boldú, J. J., Graham, D., Morooka, M., Andre, M., Khotyaintsev, Y. V., Dimmock, A., et al. (2024). Ion-acoustic waves associated with interplanetary shocks. *Geophysical Research Letters*, 51(16), e2024GL109956. <https://doi.org/10.1029/2024gl109956>
- Burch, J. L., Giles, B. L., Ahmadi, N., Argall, M. R., Baker, D. N., Blake, J. B., et al. (2024). Magnetospheric Multiscale (MMS) – Calibration and measurement algorithms document (CMAD). *Space Physics Data Facility*. <https://doi.org/10.48322/VSHD-SV21>
- Burch, J. L., Moore, T., Torbert, R., & Giles, B. (2016). Magnetospheric Multiscale overview and science objectives. *Space Science Reviews*, 199(1–4), 5–21. <https://doi.org/10.1007/s11214-015-0164-9>
- Burgess, D., & Scholer, M. (2015). Collisionless shocks in space plasmas: Structure and accelerated particles.
- Burlaga, L., Sittler, E., Mariani, F., & Schwenn, a. R. (1981). Magnetic loop behind an interplanetary shock: Voyager, helios, and imp 8 observations. *Journal of Geophysical Research*, 86(A8), 6673–6684. <https://doi.org/10.1029/ja086ia08p06673>
- Cohen, I. J., Schwartz, S. J., Goodrich, K. A., Ahmadi, N., Ergun, R. E., Fuselier, S. A., et al. (2019). High-resolution measurements of the cross-shock potential, ion reflection, and electron heating at an interplanetary shock by mms. *Journal of Geophysical Research: Space Physics*, 124(6), 3961–3978. <https://doi.org/10.1029/2018JA026197>

- De Lucas, A., Schwenn, R., Dal Lago, A., Marsch, E., & de Gonzalez, A. C. (2011). Interplanetary shock wave extent in the inner heliosphere as observed by multiple spacecraft. *Journal of Atmospheric and Solar-Terrestrial Physics*, 73(10), 1281–1292. <https://doi.org/10.1016/j.jastp.2010.12.011>
- Dimmock, A. P., Gedalin, M., Lalti, A., Trotta, D., Khotyaintsev, Y. V., Graham, D. B., et al. (2023). Backstreaming ions at a high mach number interplanetary shock-solar orbiter measurements during the nominal mission phase. *Astronomy and Astrophysics*, 679, A106. <https://doi.org/10.1051/0004-6361/202347006>
- Dimmock, A. P., Yordanova, E., Graham, D. B., Khotyaintsev, Y. V., Blanco-Cano, X., Kajdič, P., et al. (2022). Mirror mode storms observed by solar orbiter. *Journal of Geophysical Research: Space Physics*, 127(11), e2022JA030754. <https://doi.org/10.1029/2022ja030754>
- Dmitriev, A., Crosby, N., & Chao, J.-K. (2005). Interplanetary sources of space weather disturbances in 1997 to 2000. *Space Weather*, 3(3). <https://doi.org/10.1029/2004sw000104>
- Dryer, M. (1973). Bow shock and its interaction with interplanetary shocks. *Radio Science*, 8(11), 893–901. <https://doi.org/10.1029/rs008i011p00893>
- Ergun, R. (2022). MMS 1 electric double probe (EDP) three-dimensional electric field, level 2 (L2), burst mode, 0.1220703125 ms data [Dataset]. *NASA Space Physics Data Facility*. <https://doi.org/10.48322/rxbn-r719>
- Ergun, R., Tucker, S., Westfall, J., Goodrich, K., Malaspina, D., Summers, D., & others (2016). The axial double probe and fields signal processing for the mms mission. *Space Science Reviews*, 199, 167–188.
- Fedorov, A. (2020). Swa-pas l2 data user guide. Retrieved from [https://www.cosmos.esa.int/documents/3689933/11863901/PAS\\_L2\\_Data\\_User\\_Guide\\_20201116.pdf/ed680576-83fb-2f20-737e-9e8c46fefeb60?t=1679313350405](https://www.cosmos.esa.int/documents/3689933/11863901/PAS_L2_Data_User_Guide_20201116.pdf/ed680576-83fb-2f20-737e-9e8c46fefeb60?t=1679313350405)
- Gary, S. P. (1978). Ion-acoustic-like instabilities in the solar wind. *Journal of Geophysical Research*, 83(A6), 2504–2510. <https://doi.org/10.1029/JA083iA06p02504>
- Gary, S. P. (1993). *Theory of space plasma microinstabilities (No. 7)*. Cambridge University Press
- Gedalin, M. (2015). Collisionless relaxation of non-gyrotropic downstream ion distributions: Dependence on shock parameters. *Journal of Plasma Physics*, 81, 905810603. <https://doi.org/10.1017/S0022377815001154>
- Gedalin, M. (2016). Downstream plasma parameters in laminar shocks from ion kinetics. *Physics of Plasmas*, 23(10), 102904. <https://doi.org/10.1063/1.4966240>
- Gedalin, M. (2017). Effect of alpha particles on the shock structure. *Journal of Geophysical Research: Space Physics*, 122(1), 71–76. <https://doi.org/10.1002/2016JA023460>
- Gedalin, M. (2019). Kinematic collisionless relaxation and time dependence of supercritical shocks with alpha particles. *The Astrophysical Journal*, 880(2), 140. <https://doi.org/10.3847/1538-4357/ab2bee>
- Gedalin, M., Friedman, Y., & Balikhin, M. (2015). Collisionless relaxation of downstream ion distributions in low-mach number shocks. *Physics of Plasmas*, 22(7), 072301. <https://doi.org/10.1063/1.4926452>
- Gedalin, M., Zhou, X., Russell, C. T., Drozdov, A., & Liu, T. Z. (2018). Ion dynamics and the shock profile of a low-mach number shock. *Journal of Geophysical Research: Space Physics*, 123(11), 8913–8923. <https://doi.org/10.1029/2018JA025945>
- Gershman, D. J., Giles, L., Barbara, P. J., Craig, M., Thomas, E., & Burch, L. J. (2022a). MMS 1 fast plasma investigation, dual ion spectrometer (FPI, DIS) distribution moments, level 2 (L2), burst mode, 0.15 s data [Dataset]. *NASA Space Physics Data Facility*. <https://doi.org/10.48322/qggf-vr83>
- Gershman, D. J., Giles, L., Barbara, P. J., Craig, M., Thomas, E., & Burch, L. J. (2022b). MMS 1 fast plasma investigation, dual ion spectrometer (FPI, DIS) instrument distributions, level 2 (L2), burst mode, 0.15 s data [Dataset]. *NASA Space Physics Data Facility*. <https://doi.org/10.48322/dq1y-nf73>
- Gopalswamy, N., Mäkelä, P., Yashiro, S., Akiyama, S., & Xie, H. (2022). Solar activity and space weather. *Journal of Physics: Conference Series*, 2214(1), 12021. <https://doi.org/10.1088/1742-6596/2214/1/012021>
- Graham, D. B. (2024). The structure and kinetic ion behavior of low mach number shocks (v1.0.1) [Software]. *Zenodo*. <https://doi.org/10.5281/zenodo.13732516>
- Graham, D. B., & Khotyaintsev, Y. V. (2025). The structure and kinetic ion behavior of low mach number shocks. *Journal of Geophysical Research: Space Physics*, 130(5), e2024JA033283. <https://doi.org/10.1029/2024ja033283>
- Graham, D. B., Khotyaintsev, Y. V., Dimmock, A. P., Lalti, A., Boldú, J. J., Tigik, S. F., & Fuselier, S. A. (2024). Ion dynamics across a low mach number bow shock. *Journal of Geophysical Research: Space Physics*, 129(4), e2023JA032296. <https://doi.org/10.1029/2023JA032296>
- Graham, D. B., Khotyaintsev, Y. V., & Lalti, A. (2025). Ion-acoustic waves and the proton-alpha streaming instability at collisionless shocks. *Geophysical Research Letters*, 52(9), e2025GL115273. <https://doi.org/10.1029/2025gl115273>
- Gurnett, D. A., & Bhattacharjee, A. (2017). *Introduction to plasma physics: With space, laboratory and astrophysical applications* (2nd ed.). Cambridge University Press.
- Horbury, T. S. (2020). MAG, solar Orbiter magnetometer, level 2 (L2) MAG normal mode magnetic field in RTN coordinates (L2-mag-rtn-normal) [Dataset]. *European Space Agency*. <https://doi.org/10.5270/esa-ux7y320>
- Horbury, T. S., O'Brien, H., Blazquez, I. C., Bendyk, M., Brown, P., Hudson, R., et al. (2020). The solar orbiter magnetometer. *Astronomy and Astrophysics*, 642, A9. <https://doi.org/10.1051/0004-6361/201937257>
- Kajdič, P., Blanco-Cano, X., Aguilar-Rodríguez, E., Russell, C. T., Jian, L. K., & Luhmann, J. G. (2012). Waves upstream and downstream of interplanetary shocks driven by coronal mass ejections. *Journal of Geophysical Research*, 117(A6). <https://doi.org/10.1029/2011JA017381>
- Kennel, C., Edmiston, J., & Hada, T. (1985). A quarter century of collisionless shock research. *Geophysical Monograph Series*, 34, 1–36.
- Khotyaintsev, Y. V., Graham, D. B., & Johlander, A. (2024). Ion reflection by a rippled perpendicular shock. *Physical Review Letters*, 133(21), 215201. <https://doi.org/10.1103/physrevlett.133.215201>
- Khotyaintsev, Y. V., Graham, D. B., Vaivads, A., Steinvall, K., Edberg, N. J. T., Eriksson, A. I., et al. (2021). Density fluctuations associated with turbulence and waves. *Astronomy and Astrophysics*, 656, A19. <https://doi.org/10.1051/0004-6361/202140936>
- Khotyaintsev, Y. V., Vaivads, A., Retinò, A., André, M., Owen, C., & Nilsson, H. (2006). Formation of inner structure of a reconnection separatrix region. *Physical Review Letters*, 97(20), 205003. <https://doi.org/10.1103/physrevlett.97.205003>
- Khrabrov, A., & Sonnerup, B. Ö. (1998). Error estimates for minimum variance analysis. *Journal of Geophysical Research*, 103(A4), 6641–6651. <https://doi.org/10.1029/97ja03731>
- Lalti, A., Khotyaintsev, Y. V., & Graham, D. B. (2023). Short-wavelength electrostatic wave measurement using mms spacecraft. *Journal of Geophysical Research: Space Physics*, 128(4), e2022JA031150. <https://doi.org/10.1029/2022ja031150>
- Lalti, A., Khotyaintsev, Y. V., Dimmock, A. P., Johlander, A., Graham, D. B., & Olshevsky, V. (2022). A database of mms bow shock crossings compiled using machine learning. *Journal of Geophysical Research: Space Physics*, 127(8), e2022JA030454. <https://doi.org/10.1029/2022ja030454>

- Lindqvist, P.-A., Olsson, G., Torbert, R., King, B., Granoff, M., Rau, D., & others (2016). The spin-plane double probe electric field instrument for mms. *Space Science Reviews*, 199, 137–165.
- Liu, Z., Zhao, J., Sun, H., Xiang, L., Liu, W., Lu, J., & Zhou, W. (2019). Parallel-propagating waves and instabilities in plasmas with streaming proton and alpha particles. *The Astrophysical Journal*, 874(2), 128. <https://doi.org/10.3847/1538-4357/ab0896>
- Maksimovic, M. (2020). (RPW, radio and plasma waves instrument, level 2 (L2) TDS electric field triggered snapshot waveforms (rpw-tds-surv-tswf-e) and STAT statistical product of electric field continuous snapshots [Dataset]. *European Space Agency*. <https://doi.org/10.57780/esa-3x-cjd4w>
- Maksimovic, M., Bale, S. D., Chust, T., Khotyaintsev, Y., Krasnoselskikh, V., Kretschmar, M., et al. (2020). The solar orbiter radio and plasma waves (rpw) instrument (Vol. 17).
- Müller, D., Cyr, O. C. S., Zouganelis, I., Gilbert, H. R., Marsden, R., Nieves-Chinchilla, T., et al. (2020). The solar orbiter mission. *Astronomy and Astrophysics*, 642, A1. <https://doi.org/10.1051/0004-6361/202038467>
- Odstrcil, D., Riley, P., & Zhao, X. (2004). Numerical simulation of the 12 may 1997 interplanetary cme event. *Journal of Geophysical Research*, 109(A2). <https://doi.org/10.1029/2003ja010135>
- Ofman, L., Balikhin, M., Russell, C. T., & Gedalin, M. (2009). Collisionless relaxation of ion distributions downstream of laminar quasi-perpendicular shocks. *Journal of Geophysical Research*, 114(A9). <https://doi.org/10.1029/2009JA014365>
- Owen, C. J. (2020). (The solar orbiter solar wind analyser (SWA) suite, level 2 (L2) PAS velocity distribution functions (swa-pas-vdf), PAS ground calculated moments (swa-pas-grnd-mom) and EAS single strahl electron distribution data product (eas[1/2]-ss-psd) [Dataset]. *European Space Agency*. <https://doi.org/10.5270/esa-ahypgn6>
- Owen, C. J., Bruno, R., Livi, S., Louarn, P., Janabi, K. A., Allegrini, F., et al. (2020). The solar orbiter solar wind analyser (swa) suite. *Astronomy and Astrophysics*, 642, A16. <https://doi.org/10.1051/0004-6361/201937259>
- Pollock, C., Moore, T., Jacques, A., Burch, J., Gliese, U., Saito, Y., et al. (2016). Fast plasma investigation for magnetospheric multiscale. *Space Science Reviews*, 199(1–4), 331–406. <https://doi.org/10.1007/s11214-016-0245-4>
- Pope, S., Gedalin, M., & Balikhin, M. (2019). The first direct observational confirmation of kinematic collisionless relaxation in very low mach number shocks near the earth. *Journal of Geophysical Research: Space Physics*, 124(3), 1711–1725. <https://doi.org/10.1029/2018ja026223>
- Pulupa, M., Bale, S., & Kasper, J. (2010). Langmuir waves upstream of interplanetary shocks: Dependence on shock and plasma parameters. *Journal of Geophysical Research*, 115(A4). <https://doi.org/10.1029/2009ja014680>
- Reames, D. V. (2001). Seps: Space weather hazard in interplanetary space. *Geophysical Monograph-American Geophysical Union*, 125, 101–108.
- Roberts, O., Nakamura, R., Coffey, V., Gershman, D., Volwerk, M., Varsani, A., et al. (2021). A study of the solar wind ion and electron measurements from the magnetospheric multiscale mission's fast plasma investigation. *Journal of Geophysical Research: Space Physics*, 126(10), e2021JA029784. <https://doi.org/10.1029/2021ja029784>
- Russell, C. T. (2022). MMS 1 flux gate magnetometer (FGM) DC magnetic field, level 2 (L2), burst mode, 128 Sample/s, v4/5 data [Dataset]. *NASA Space Physics Data Facility*. <https://doi.org/10.48322/pj0n-m695>
- Russell, C. T., Anderson, B. J., Baumjohann, W., Bromund, K. R., Dearborn, D., Fischer, D., & others (2016). The magnetospheric multiscale magnetometers. *Space Science Reviews*, 199, 189–256.
- Russell, C. T., Jian, L. K., Blanco-Cano, X., & Luhmann, J. G. (2009). Stereo observations of upstream and downstream waves at low mach number shocks. *Geophysical Research Letters*, 36(3). <https://doi.org/10.1029/2008GL036991>
- Santolík, O., Parrot, M., & Lefeuvre, F. (2003). Singular value decomposition methods for wave propagation analysis. *Radio Science*, 38(1), 10–1. <https://doi.org/10.1029/2000rs002523>
- Smith, E. J., & Burton, M. E. (1988). Shock analysis: Three useful new relations. *Journal of Geophysical Research*, 93(A4), 2730–2734. <https://doi.org/10.1029/JA093iA04p02730>
- Soucek, J., & Escoubet, C. P. (2011). Cluster observations of trapped ions interacting with magnetosheath mirror modes. *Annales Geophysicae*, 29(6), 1049–1060. <https://doi.org/10.5194/angeo-29-1049-2011>
- Soucek, J., Piša, D., Kolmasova, I., Uhlir, L., Lan, R., Santolík, O., et al. (2021). Solar orbiter radio and plasma waves - Time domain sampler: In-flight performance and first results. *Astronomy and Astrophysics*, 656, A26. <https://doi.org/10.1051/0004-6361/202140948>
- Trotta, D., Dimmock, A., Hietala, H., Blanco-Cano, X., Horbury, T. S., Vainio, R., et al. (2025). An overview of solar orbiter observations of interplanetary shocks in solar cycle 25. *The Astrophysical Journal Supplement Series*, 277(1), 2. <https://doi.org/10.3847/1538-4365/ada4a7>
- Tsurutani, B. T., Smith, E. J., & Jones, D. E. (1983). Waves observed upstream of interplanetary shocks. *Journal of Geophysical Research*, 88(A7), 5645–5656. <https://doi.org/10.1029/JA088iA07p05645>
- Vech, D., Szego, K., Opitz, A., Kajdic, P., Fraenz, M., Kallio, E., & Alho, M. (2015). Space weather effects on the bow shock, the magnetic barrier, and the ion composition boundary at Venus. *Journal of Geophysical Research: Space Physics*, 120(6), 4613–4627. <https://doi.org/10.1002/2014ja020782>
- Vogt, J., Haaland, S., & Paschmann, G. (2011). Accuracy of multi-point boundary crossing time analysis. *Annales Geophysicae*, 29(12), 2239–2252. <https://doi.org/10.5194/angeo-29-2239-2011>
- Wilson, L. B., III. (2016). Low frequency waves at and upstream of collisionless shocks. *Low-frequency waves in space plasmas*, 269–291.
- Wilson, L. B., III, Cattell, C., Kellogg, P. J., Goetz, K., Kersten, K., Hanson, L., et al. (2007). Waves in interplanetary shocks: A wind/waves study. *Physical Review Letters*, 99(4), 041101. <https://doi.org/10.1103/PhysRevLett.99.041101>
- Wilson, L. B., Koval, A., Szabo, A., Breneman, A., Cattell, C. A., Goetz, K., et al. (2012). Observations of electromagnetic whistler precursors at supercritical interplanetary shocks. *Geophysical Research Letters*, 39(8). <https://doi.org/10.1029/2012GL051581>
- Wu, C., Winske, D., Zhou, Y., Tsai, S., Rodriguez, P., Tanaka, M., et al. (1984). Microinstabilities associated with a high mach number, perpendicular bow shock. *Space Science Reviews*, 37(1–2), 63–109. <https://doi.org/10.1007/bf00213958>
- Young, D., Burch, J., Gomez, R., De Los Santos, A., Miller, G., Wilson IV, P., et al. (2016). Hot plasma composition analyzer for the magnetospheric multiscale mission. *Space Science Reviews*, 199(1), 407–470. <https://doi.org/10.1007/s11214-014-0119-6>
- Zank, G., Li, G., & Verkhoglyadova, O. (2007). Particle acceleration at interplanetary shocks. *Space Science Reviews*, 130(1–4), 255–272. <https://doi.org/10.1007/s11214-007-9214-2>